3D Porous N-Doped Graphene Frameworks Made of Interconnected Nanocages for Ultrahigh-Rate and Long-Life Li–O_2 Batteries

*Changtai Zhao, Chang Yu, Shaohong Liu, Juan Yang, Xiaoming Fan, Huawei Huang, and Jieshan Qiu**

The inferior rate capability and poor cycle stability of the present Li–O_2 batteries are still critical obstacles for practice applications. Configuring novel and integrated air electrode materials with unique structure and tunable chemical compositions is one of the efficient strategies to solve these bottleneck problems. Herein, a novel strategy for synthesis of 3D porous N-doped graphene aerogels (NPGAs) with frameworks constructed by interconnected nanocages with the aid of polystyrene sphere@polydopamine is reported. The interconnected nanocages as the basic building unit of graphene sheets are assembled inside the skeletons of 3D graphene aerogels, leading to the 3D NPGA with well-developed interconnected channels and the full exposure of electrochemically active sites. Benefiting from such an unique structure, the as-made NPGA delivers a high specific capacity, an excellent rate capacity of 5978 mA h g^{-1} at 3.2 A g^{-1}, and long cycle stability, especially at a large current density (54 cycles at 1 A g^{-1}), indicative of boosted rate capability and cycle life as air electrodes for Li–O_2 batteries. More importantly, based on the total mass of C+Li_2O_2, a gravimetric energy density of 2400 W h kg^{-1} for the NPGA–O_2//Li cell is delivered at a power density of 1300 W kg^{-1}.

1. Introduction

Electrochemical energy storage is a key technology for utilization of renewable energy resources to achieve the clean and sustainable mobile energy supply.[1] Of the energy storage devices, Li–O_2 batteries with an ultrahigh theoretical energy density of ca. 3500 W h kg^{-1} (based on the mass of Li and O_2) have triggered worldwide research interests and become one of the most potential candidates for powering the electric vehicles (EVs) and hybrid electric vehicles (HEVs).[2] However, the Li–O_2 batteries are facing several challenges for use in EVs/HEVs, which are low round-trip efficiency, inferior power density (rate capability), and poor cycle life, especially at high-power density.[3] One option to tackle these challenges is to configure novel air electrode materials with unique structure and chemical compositions.[4] In general, advanced cathode materials for Li–O_2 batteries should have interconnected channels for fast supply and transportation of O_2 and Li^+, excellent conductivity for rapid electron transport, large void volume for storage of discharge products, and enough active sites for fast reaction kinetics.[5] In this respect, graphene has received considerable attention as one of the ideal candidates for Li–O_2 batteries due to its extraordinary properties including superior conductivity, large surface area, and excellent mechanical flexibility.[6]

It was reported that 3D aerogels made of assembled graphene with a wide distribution of pore size, free-standing structure, and high electrical conductivity hold a great promise for Li–O_2 batteries.[7] It is commonly believed that the morphology, structure, and chemical composition of graphene inside the skeletons of the 3D graphene aerogels are responsible for the electrochemical performance of the energy storage devices to a great degree. Duan and co-workers[8] reported that graphene hydrogels with high specific surface area were able to boost the electrochemical performance for supercapacitors due to the elaborated combination of surface functionalization and hierarchical structures of graphene sheets. Qu and co-workers[7d,9] developed a polypyrrole-mediated technique to fabricate graphene aerogels that feature a unique 3D porous structure and highly exposed graphene sheets with less stacking, which have shown an ultralow density and excellent electrochemical performance for supercapacitors. In the case of high-performance Li–O_2 batteries, the electrode materials with interconnected macropore channels, large void volume, and high specific surface area are highly demanded.[4d,10] For the graphene aerogels, how to further tailor the structure and properties of the skeletons within the graphene aerogels by tuning the basic building unit of graphene still remains a big challenge. Moreover, it has also been noted that the heteroatom hybridization is effective to facilitate oxygen reduction reactions (ORR) and oxygen evolution reactions (OER) due to the modulated carbon electronic structure

C. T. Zhao, Dr. C. Yu, S. H. Liu, J. Yang, Dr. X. M. Fan, H. W. Huang, Prof. J. S. Qiu
State Key Lab of Fine Chemicals
Carbon Research Laboratory
Liaoning Key Lab for Energy Materials
and Chemical Engineering
Dalian University of Technology
Dalian 116024, P.R. China
E-mail: jqiu@dlut.edu.cn

DOI: 10.1002/adfm.201503077

for enhancing oxygen adsorption and accelerating the reaction rate.[11] These interesting novel structure and composition could be combined and coupled together to make graphene electrode materials for high-performance Li–O_2 batteries.

Here, we report a facile hydrothermal self-assembly approach followed by high-temperature annealing to fabricate 3D porous N-doped graphene aerogels (NPGAs). The frameworks within the NPGA matrix are made of interconnected carbon nanocages, which are resulted from the polystyrene sphere@polydopamine (PS@PDA) that function as effective scaffolds wrapped in the skeletons of NPGA precursors. The NPGA was evaluated as free-standing air electrodes for Li–O_2 batteries, showing an ultrahigh rate capacity of 5978 mA h g^{-1} at a current density of 3.2 A g^{-1}. To our knowledge, this is the best rate capability ever reported for non-aqueous, rechargeable Li–O_2 batteries up to date. Based on the total mass of C+Li_2O_2, a gravimetric energy density of 2400 W h kg^{-1} for the NPGA-O_2//Li cell is delivered at a power density of 1300 W kg^{-1}, which is in good match with the required level of the engine-driven systems. More importantly, the NPGA air electrodes also show excellent cycle stability (72 cycles at 300 mA g^{-1}, and 54 cycles at a large current density of 1 A g^{-1}). At the same time, a low overpotential is delivered, indicative of a catalyst-like behavior. The superior electrochemical performances of the as-made NPGA is believed to be due to the interconnected porous channels, large void volume, multidimensional electron transport pathways, less stacking of graphene sheets, and the full exposure of active sites resulted from the doped N atoms within graphene sheets.

2. Results and Discussion

The NPGA was prepared by a combined strategy involving polymerization and hydrothermal step followed by heat treatment of which the schematic process is shown in **Scheme 1**. Briefly, the PS spheres were coated with PDA to make PS@PDA that functioned as scaffolds. Then, the PS@PDAs were mixed with graphene oxide (GO) to form a graphene hydrogel under hydrothermal conditions via a self-assembly scheme, resulting in the NPGA precursor (NPGA-p). The as-made NPGA-p was annealed at high temperature, yielding 3D NPGA with frameworks made of graphene nanocages that were well interconnected.

The morphology and structure of the NPGA were examined by the field emission scanning electron microscopy (FESEM) and transmission electron microscopy (TEM) of which the typical images are shown in **Figure 1**. Figure 1a shows that the NPGA is composed of the interpenetrated and cross-linked graphene sheets in which abundant macro- and micro-sized interconnected channels within the 3D frameworks can be clearly seen. This kind of porous structure is highly required for electrodes in Li–O_2 batteries, simply because the interconnected channels would function as "highways" to quickly supply O_2 and Li^+ to the skeleton surface of graphene aerogels, which are ideal for the storage and fast yet uniform distribution of the electrolyte and discharge products. The 3D interpenetrated graphene framework is robust and can function as a multidimensional conductive network to quickly transport electrons within the whole electrode matrix. The FESEM images in Figure 1b,c further reveal that the skeletons of graphene aerogels are composed of interconnected graphene nanocages, which help to prohibit graphene sheets from aggregating and restacking to some degree, thus resulting in the less stacking and the full exposure of electrochemically active sites of the graphene sheets. For Li–O_2 batteries, the well-developed porous structure made of assembled-nanocages of graphene in the skeleton and matrix is helpful for the fast transportation and distribution of O_2 and Li^+ within the electrode skeletons. The crumpled graphene sheets, combined with the embedded nanocages, would provide large yet active interfaces or tri-phase (solid–liquid–gas) regions for deposition of discharge products.[3d,4d] The TEM images of the NPGA (Figure 1d,e) further confirm that the graphene sheets in the NPGA are composed of interconnected nanocages and have a relatively crumpled and loose structure. Further HRTEM examination of the NPGA (Figure S2, Supporting Information) clearly reveals that the graphene in the NPGA is made of only a few layers of graphene sheets. More detailed examination of the nanocage units (Figure 1f) reveals that the nanocages feature a heterogeneous carbon structure, indicative of the contributions from different carbon precursors. This implies that the nanocages within NPGA matrix are mainly composed of the PDA-derived carbon and few layers of graphene sheets, also further revealed by comparing the TEM images of NPGA (Figure 1d–f) and PDA-derived carbon without GO (Figure S3, Supporting Information). For comparison, general graphene aerogels (GAs) are also prepared in the absence of PS@PDA, and the corresponding SEM and TEM

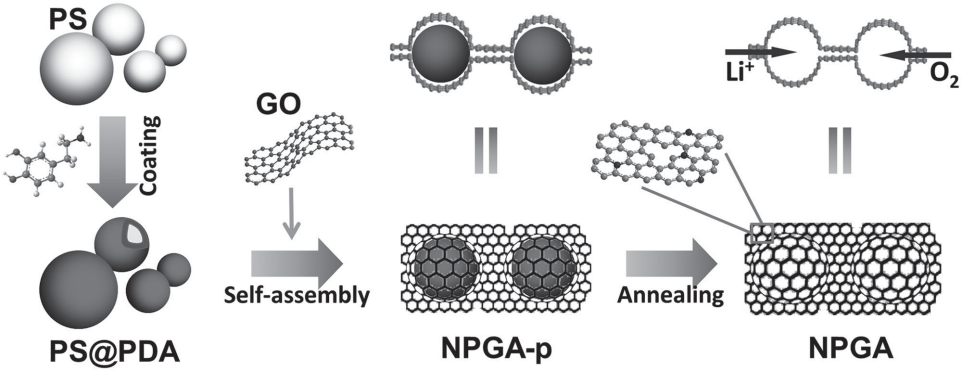

Scheme 1. Schematic process for synthesis of NPGA.

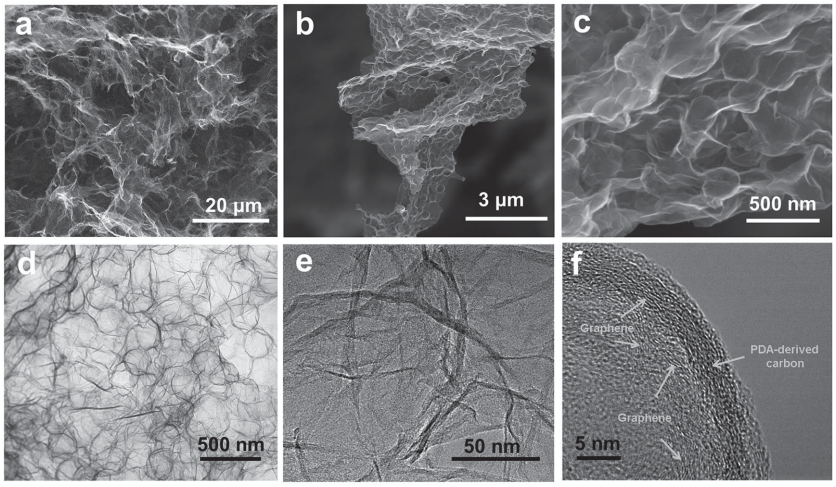

Figure 1. a–c) FESEM images of NPGA at different magnifications; d,e) TEM images of NPGA at different magnifications; f) HRTEM image of the shell for a nanocage of the NPGA.

images are shown in Figure S4 (Supporting Information). Relatively large graphene platelets composed of excessive aggregation and cross-linked graphene sheets can be clearly observed, which would decrease the effective transportation pathways and simultaneously increase the transportation distance of O_2 and Li^+ to a great degree.

The relatively loose structure within NPGA was also further confirmed and revealed by changing pore structure characteristics analyzed by nitrogen adsorption technique. From the adsorption–desorption isotherms shown in **Figure 2**a, it is noted that the N_2 adsorptive amount for NPGA is obviously higher than that of GA, and typical type II characteristics are delivered for both GA and NPGA, indicative of a wide range of pore structure.[7a,7c,7d,12] The corresponding Brunauer–Emmett–Teller specific surface area for NPGA reaches to 344 m^2 g^{-1}, which is two times higher than that of GA (165 m^2 g^{-1}). The pore-size distribution data shown in Figure 2b reveal that the wide pore distribution in a range of 4–100 nm is present in as-made NPGA. This striking difference is attributed to the restacking-inhibited effects of interconnected nanocages embedded inside graphene sheets, which is not uncommon for less-stacking graphene aerogels.[1a,6f] In this case, the abundant mesopores and macropores will be beneficial to the rapid transport of O_2 and Li^+, and the high specific area contributes to a large tri-phase (solid–liquid–gas) regions and a full exposure of active sites.

The chemical composition and structure characteristics of graphene in the NPGA were examined by a number of techniques, including X-ray diffraction (XRD), Raman and X-ray photoelectron spectroscopy (XPS). Figure 2c shows the typical XRD patterns of GO and NPGA. The characteristic diffraction peak of GO at ca. 11.7° disappears and a new broad peak at ca. 25.8° corresponding to the (002) characteristic peak of graphite appears, demonstrating the

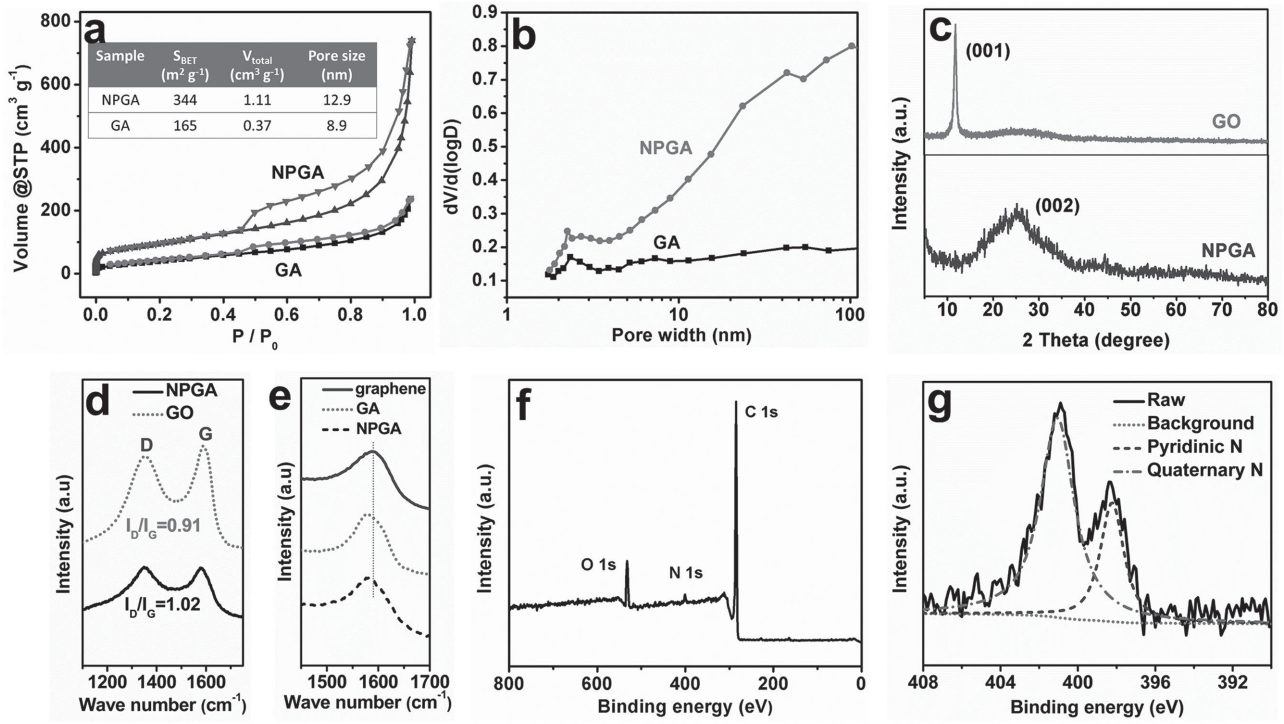

Figure 2. a) Nitrogen adsorption–desorption isotherms and b) pore-size distributions of NPGA and GA; c) XRD patterns of GO and NPGA; d) Raman spectra of GO and NPGA; e) the magnified G bands in Raman spectra for graphene, GA, and NPGA; f) XPS spectrum of NPGA and g) N 1s spectrum of NPGA.

efficient de-oxygenation of GO to form out-of-order graphene sheets along their stacking direction after hydrothermal and annealing process.[8] The Raman spectra of GO and NPGA (Figure 2d) reveal two remarkable peaks, corresponding to the D- and G-bands of carbon, respectively. It is also noted that the I_D/I_G value of NPGA (1.02) is higher than that of GO (0.91), indicating that many defects were existing in as-prepared NPGA, although the GO sheets were reduced to graphene.[13] Meanwhile, the more defects in NPGA can also be confirmed by the shift of G band from 1587 cm^{-1} for graphene without N-doping to 1576 cm^{-1} for NPGA (Figure 2e), which may be attributed to the doping effects of heteroatoms within NPGA matrix.[12] The surface chemistry and component of NPGA were further characterized by XPS. Figure 2f reveals that NPGA is mainly composed of C, N, and O elements. As shown in Figure 2g, it is clearly noted that the N 1s peaks centered at 398.2 and 401.1 eV can be assigned to two components: pyridinic and quaternary types of N atoms, respectively. The presence of N element can also be confirmed by energy-dispersive X-ray elemental mappings of NPGA (Figure S5, Supporting Information), where N atoms are uniformly distributed in NPGA matrix. The elemental analysis demonstrates that the corresponding N/C mass ratio is 4.8%. It is also found that the GA fabricated in the absence of PS@PDA has an N/C mass ratio of 4.4%. It is known that PDA is rich of N and C content, and is widely used as precursor to produce N-doped carbon materials. This implies that the N species exist within NPGA matrix made of N-doped residual carbon shell derived from PDA and N-doped graphene.

In comparison with the GA materials, the as-made NPGA features a relatively crumpled and loose structure, which helps to prohibit graphene sheets from aggregating and restacking to some degree, thus resulting in the less stacking and the full exposure of electrochemically active sites of the graphene sheets. The high specific surface area and ultrathin graphene sheets within NPGA skeletons will lead to an enhanced exposure of N atoms within graphene sheets. These integrated characteristics will be beneficial for the electrochemical reaction process in Li–O_2 batteries. The electrochemical performance of NPGA as binder-free air electrodes in Li–O_2 batteries was tested using coin cells with a tetraethylene glycol dimethyl ether (TEGDME) electrolyte containing 1 M LiTFSI, a glass fiber separator, and a slice of NPGA without the addition of any binders or conductive additives.[3c,4e,5a,14] To further evaluate the electrocatalytic activity of NPGA in Li–O_2 batteries, the galvanostatic discharge–charge and cyclic voltammetry (CV) measurements were performed within a voltage widow of 2.0–4.5 V. The initial discharge–charge profiles of Li–O_2 cells based on NPGA, GA, and Super P air electrodes with a cutoff capacity of 1000 mA h g^{-1} at the current density of 300 mA g^{-1} are displayed in **Figure 3**a. Interestingly, NPGA air electrode exhibits a relatively high discharge voltage and low charge voltage compared with that of GA and Super P air electrodes, consequently yielding an enhanced round-trip efficiency. For example, the

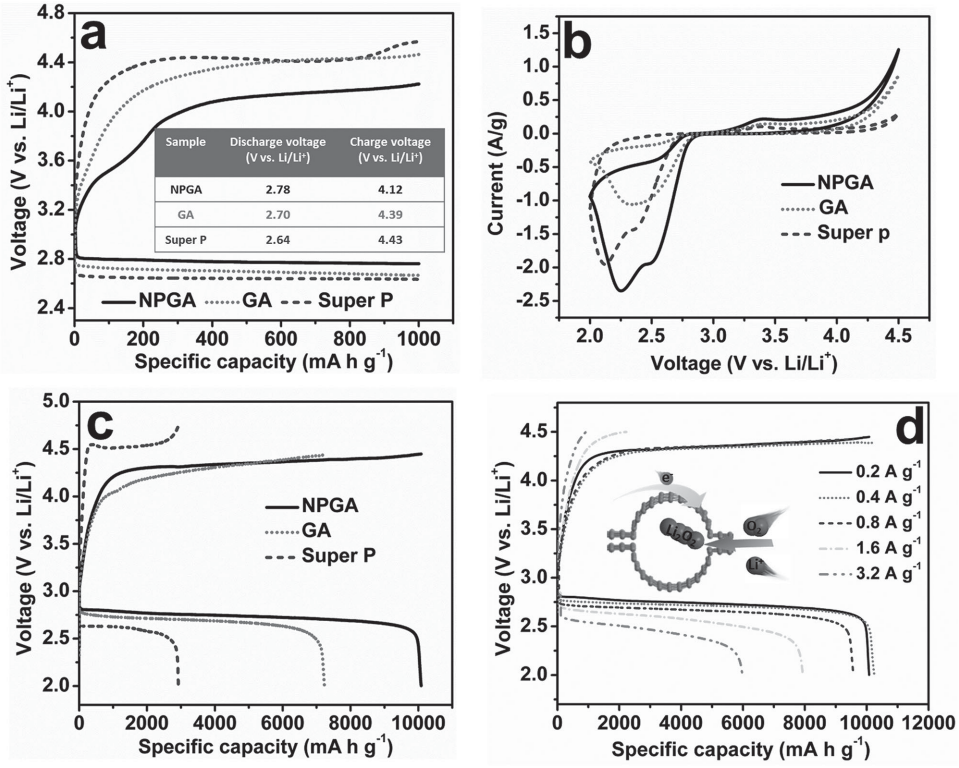

Figure 3. a) The discharge–charge curves of NPGA, GA, and Super P electrodes with a fixed capacity of 1000 mA h g^{-1} at a current density of 300 mA g^{-1}; b) the CV curves of the NPGA, GA, and Super P electrodes within a voltage widow of 2.0–4.5 V at a scanning rate of 0.1 mV s^{-1}; c) the initial discharge–charge curves of NPGA, GA, and Super P electrodes at a current density of 200 mA g^{-1}; d) the discharge curves of NPGA electrode at different current densities, inset is the schematic illustration of nanocage effects.

discharge voltage platform of NPGA air electrode is 2.78 V that is higher than that of GA (2.70 V) and Super P (2.64 V) air electrodes. More importantly, its charge voltage (4.12) is much lower than that of GA (4.39) and Super P (4.43) air electrodes, which would help to decrease the decomposition of electrolyte to some extent. The CV measurement (Figure 3b) was further used to investigate the electrochemical catalytic activity of NPGA. Compared with the GA and Super P air electrodes, the NPGA air electrode delivers higher ORR onset potential, lower OER onset potential, and higher ORR and OER peak currents, indicative of a catalyst-like behavior of NPGA and a high catalytic activity for both ORR and OER processes. Such an excellent electrochemical catalytic activity of NPGA can be attributed to the enhanced ORR and OER kinetics due to less stacking of graphene sheets and the full exposure of N atom sites within graphene sheets in the as-made NPGA.

The discharge specific capacity of NPGA air electrode was examined by the galvanostatic discharge–charge test. As shown in Figure 3c, at a current density of 200 mA g^{-1}, NPGA air electrode delivers a specific capacity of 10 081 mA h g^{-1}, which is higher than 7230 mA h g^{-1} of GA and 2923 mA h g^{-1} of Super P air electrodes. Surprisingly, with the increase of the current density, the NPGA air electrode is capable of delivering high specific capacity, evidenced by the high value of 5978 mA h g^{-1} delivered at a high current density of 3.2 A g^{-1} (Figure 3d), and to the best of our knowledge, this is the best rate performance that has been reported so far for nonaqueous, rechargeable Li–O_2 batteries. **Figure 4**a shows the comparison of the rate performance of air electrode materials between the present work and previous work in the literature.[3d,5b,10c,11b,15] Benefiting from well-developed interconnected channels, the NPGA holds promise as air electrode materials for Li–O_2 batteries with both high energy density and high power density. Based on the total mass of C+Li_2O_2, the gravimetric energy density of NPGA-O_2//Li cell reaches to 2400 W h kg^{-1} at a power density of 1300 W kg^{-1}, indicating the significant advantages of high energy density and high power density compared with Ni–MH batteries and Li–ion battery, which is also in good match with the requirements for engine-driven systems (shown in Figure 4b).[16]

The cycling performance of the batteries is another big concern for practical applications. We have examined the cycling performance of the Li–O_2 cell with NPGA as air electrode of which the results are shown in **Figure 5**a. It can be seen clearly that the NPGA air electrode can be cycled 72 cycles with no capacity loss, with a cutoff capacity of 1000 mA h g^{-1} at a high current density of 300 mA g^{-1}, which is longer than 32 cycles of GA air electrode and 6 cycles of Super P air electrode. The corresponding discharge–charge profiles further reveal that there is almost no degradation of discharge and charge profiles for the Li–O_2 cells based on NPGA air electrode after 60 cycles (as shown in Figure 5b), which is superior to that of GA and Super P air electrodes (Figure 5c,d). To explore the potential of this kind of batteries for high-power EVs/HEVs, we further evaluated the cycling stability of NPGA air electrode at a large current density of 1 A g^{-1}, corresponding to an initial energy density of 1451 W h kg^{-1} and a power density of 1451 W kg^{-1} (Figure 5e and Figure S6 in the Supporting Information). The ca. 60% round-trip efficiency is achieved. The reason for this is attributed to the high charge voltage that was caused by the serious polarization of charge reaction at a high current density (Figure 5e). This is also a common issue needed to be addressed and solved in Li–O_2 batteries. Interestingly, the Li–O_2 cell with NPGA air electrode can be stable for 54 cycles, which is much better than the performance of the rechargeable Li–O_2 batteries reported up to now in the literature. Compared with the metal-free cathodes reported in recent literature (for details, please refer to Table S1, Supporting Information), the cycling performance of NPGA air electrode is superior to other pure graphene cathodes.

Such a superior electrochemical performance was further confirmed by Nyquist plots (Figure 5f) and its fitted results of equivalent circuits (Figure S7, Supporting Information). It can be clearly seen from Figure 5f that the diameter of the semicircle in the high-medium frequency region of the electrodes adopted follows in the order of NPGA < GA < Super P. This implies that the NPGA air electrode delivers the lowest charge-transfer impedance R_{ct} (82.0 Ω) in comparison to those of the GA (141.1 Ω) and Super P (478.1 Ω) air electrodes due to the 3D conductive network and the hierarchically interconnected channels. For the detailed information, please refer to the equivalent electric circuit and data shown in Figure S7 in the Supporting Information.

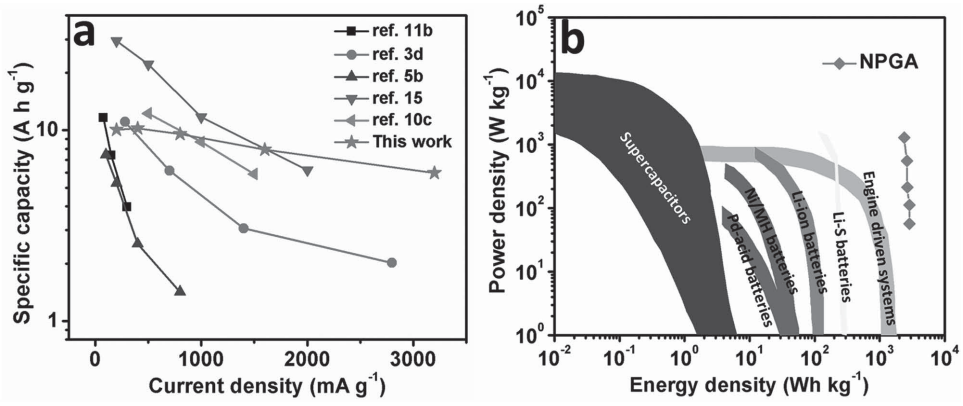

Figure 4. a) A comparison of the rate performance of air electrode materials in the present work and previous work in literature; b) Ragone plot of the Li–O_2 batteries with NPGA as air electrode (based on the total mass of C + Li_2O_2), and other energy storage devices (based on total mass of packaged device).

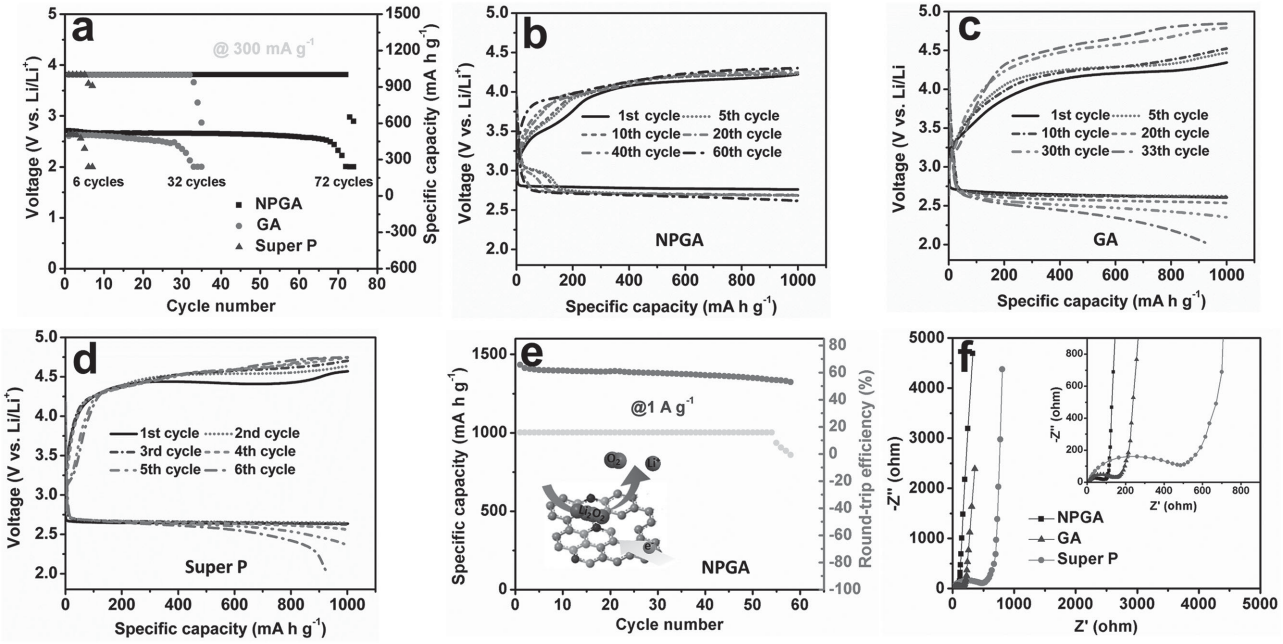

Figure 5. a) Discharge capacity and the discharge terminal voltage versus the cycle number for Li–O_2 cells with NPGA, GA, and Super P air electrodes at 300 mA g^{-1}; the discharge–charge profiles of b) NPGA, c) GA, and d) Super P air electrodes with different cycles; e) discharge capacity and round-trip efficiency versus the cycle number for Li–O_2 cell with NPGA air electrode at 1 A g^{-1}, inset is the schematic illustration of N-doped graphene effect during charge; f) Nyquist plots of Li–O_2 cells with NPGA, GA, and Super P air electrodes, inset is the magnified Nyquist plots.

In order to further work out the reasons for the high activity and long cycle life of NPGA air electrodes, the morphology and structure of the NPGA electrodes after discharge and charge were analyzed by FESEM of which the detailed results are shown in Figure S8 in the Supporting Information. It can be seen that the discharge products are uniformly deposited on the surface of NPGA like a piece of film (Figure S8a, Supporting Information), and are composed of Li_2O_2 and a little of LiOH (Figure S9, Supporting Information).[4d] After charge, it is interesting to note that these products can almost completely be decomposed, and the original structure of the NPGA air electrode is recovered (Figure S8b, Supporting Information), which is also further confirmed by the corresponding electrochemical impedance spectra (EIS, Figure S10, Supporting Information), Fourier transform infrared spectroscopy (FTIR, Figure S11, Supporting Information), and TEM (Figure S12, Supporting Information) results before and after charge. The reversible formation and decomposition of the discharge products have ensured the high electrocatalytic activity and excellent cycle stability of the Li–O_2 cells with the NPGA air electrode.

These encouraging results have demonstrated the versatile advantages of NPGA as air electrode in Li–O_2 batteries in terms of the enhanced round-trip efficiency, high power density, and long cycle life, especially the high-power cycle life. Below is the possible reasons for this: (1) the abundant macropores and interconnected porous channels of graphene aerogels can store much more electrolytes, facilitate the fast and uniform transportation of O_2 and Li^+ to the skeleton surface of graphene aerogels, and provide a large space to accommodate the discharge products; (2) the 3D interpenetrating graphene framework can achieve the rapid and multidimensional transport of electrons in the whole electrode network;[5b,14,17] (3) interconnected nanocages embedded in the graphene sheets that lead to relatively loose and crumpled graphene sheets help to further tailor the transportation and distribution of O_2 and Li^+ in the skeletons of graphene aerogels, thus offer a high specific surface area to ensure a large tri-phase (solid–liquid–gas) regions; (4) the full exposure and uniform distribution of N atoms within graphene sheets derived from relatively loose and crumpled structure may act as an effective catalyst for accelerating the electrode processes.

3. Conclusion

In summary, 3D porous N-doped graphene frameworks constructed by interconnected nanocage frameworks have been designed and successfully prepared. The nanocages embedded inside graphene sheets function to modulate the structure of graphene in the skeletons of graphene aerogels for achieving the high specific surface area, well-developed interconnected channels, crumpled graphene sheets, and full exposure of N atom sites. Benefiting from these unique characteristics, the Li–O_2 cells with NPGA air electrode exhibit a high specific capacity and the best rate performance compared with other materials reported in the literature. The NPGA air electrode can deliver a low overpotential and an excellent cycle stability, especially at a large current density. Based on the total mass of C + Li_2O_2, a gravimetric energy density of 2400 W h kg^{-1} at a power density of 1300 W kg^{-1} is delivered, which is near the level of engine-driven systems. The present study demonstrates an effective method for modulating and tailoring the skeletons of graphene

aerogels, which may open a new way for configuring the air electrode materials for high-power and long-life Li–O_2 batteries.

4. Experimental Section

Material Preparation: All reagents used in the present work were of analytical grade and were used without further purification. The GO was fabricated from the natural graphite by a modified Hummer's method.[18] The PS sphere (ca. 230 nm) colloidal was prepared by surfactant-free emulsion polymerization.[19]

Synthesis of PS Sphere@PDA: For a typical run, 20 mL of 30 mg mL^{-1} PS sphere colloid was diluted to 100 mL with deionized water followed by 10 min ultrasonic treatment to form a stable dispersion solution. Subsequently, 0.2 g dopamine and 0.2 g tris(hydroxymethyl) aminomethane were added into the dispersion solution under stirring. The dispersion solution was subjected to continuous magnetic stirring at room temperature for 24 h. After that, the PS sphere@PDA was yielded by filtering and washing with a large amount of deionized water. Finally, the as-made PS sphere@PDA was dispersed to a dispersion solution of 12 mg mL^{-1} (based on mass of PS sphere) under strong ultrasonic stirring for 20 min.

Synthesis of NPGA and GA: Typically, 5 mL of 6 mg mL^{-1} GO aqueous solution, 10 mL of 12 mg mL^{-1} PS sphere@PDA dispersion solution, and 0.5 g thiourea were mixed together under vigorously magnetic stirring, then the pH of the resultant solution was adjusted to 10 by adding a trace amount of ammonia solution. Finally, it was transferred into a Teflon-lined stainless-steel autoclave of 20 mL and kept at 160 °C for 15 h, yielding the NPGA-p. After freeze-drying, a simple annealing was conducted at 1000 °C for 2 h in N_2 atmosphere with a ramping rate of 2 °C min^{-1}, yielding the final product. For comparison, GA was also fabricated in the absence of PS spheres@PDA under the same conditions.

Materials Characterization: Morphology of the as-made samples was characterized with FESEM (FEI QUANTA 450 at 30 kV), TEM (Tecnai G220), and HRTEM (FEI TF30). The XRD measurements were taken on a D/Max-III-type X-ray spectrometer with Cu Kα radiation (λ = 1.5406 Å). Raman spectra were conducted on a RENISHAW inVia Raman microscope. The XPS (Thermo ESCALAB 250) measurement was performed to analyze the surface properties quantitatively. N_2 adsorption/desorption isotherms were measured with a Micromeritics 3Flex 3500. The composites were degassed at 250 °C for 5 h prior to the nitrogen adsorption measurement. Zeta potential was tested using a ZETASIZER nano series Nano-ZS90. The N content within the graphene matrix was analyzed by an elemental analyzer (vario EL III).

Electrochemical Tests: The Li–O_2 cells were assembled with a lithium foil, electrolyte (1 M LiTFSI in TEGDME), a glass fiber separator, and a porous cathode (NPGA, GA, or Super P). The porous cathodes of NPGA and GA were prepared by cutting the aerogel into slices with a diameter of ca. 1.0 cm and mass loading of ca. 0.61 mg cm^{-2}, which were directly used as the air electrodes without any auxiliary binders. The Super P cathode was prepared by casting slurry, consisting of 90% Super P and 10% polyvinylidene difluoride binder in *N*-methyl-2-pyrrolidone onto a carbon paper current collector which was dried at 120 °C for 12 h in vacuum oven. The assembly of the Li–O_2 cell was conducted using 2025-type coin cells in an argon-filled glove box followed by an overnight aging treatment before the test. The galvanostatic discharge–charge measurement of cells was performed by using a Land CT2001A battery-testing system in 1 atm O_2 at 25 °C. The EIS and CV tests were performed on a Bio-Logic VSP electrochemical workstation with the frequency range between 100 KHz and 0.01 Hz at open circuit potential and a voltage widow of 2.0–4.5 V at a scan rate of 0.1 mV s^{-1}, respectively.

Supporting Information

Supporting Information is available from the Wiley Online Library or from the author.

Acknowledgements

C.T.Z. and C.Y. contributed equally to this work. This work was partly supported by the NSFC (Nos. 21361162004 and 21522601) and the Education Department of the Liaoning Province of China (No. T2013001).

Received: July 24, 2015
Revised: September 6, 2015
Published online: October 19, 2015

[1] a) B. G. Choi, M. Yang, W. H. Hong, J. W. Choi, Y. S. Huh, *ACS Nano* **2012**, *6*, 4020; b) J. H. Lee, N. Park, B. G. Kim, D. S. Jung, K. Im, J. Hur, J. W. Choi, *ACS Nano* **2013**, *7*, 9366.

[2] a) P. G. Bruce, S. A. Freunberger, L. J. Hardwick, J. M. Tarascon, *Nat. Mater.* **2012**, *11*, 19; b) S. H. Oh, R. Black, E. Pomerantseva, J. Lee, L. F. Nazar, *Nat. Chem.* **2012**, *4*, 1004; c) K. G. Gallagher, S. Goebel, T. Greszler, M. Mathias, W. Oelerich, D. Eroglu, V. Srinivasan, *Energy Environ. Sci.* **2014**, *7*, 1555; d) H. Wang, Y. Yang, Y. Liang, G. Zheng, Y. Li, Y. Cui, H. Dai, *Energy Environ. Sci.* **2012**, *5*, 7931.

[3] a) J. J. Xu, D. Xu, Z. L. Wang, H. G. Wang, L. L. Zhang, X. B. Zhang, *Angew. Chem. Int. Ed.* **2013**, *52*, 3887; b) H. Lim, H. Song, J. Kim, H. Gwon, Y. Bae, K. Park, J. Hong, H. Kim, T. Kim, Y. H. Kim, X. Lepro, R. O. Robles, R. H. Baughman, K. Kang, *Angew. Chem. Int. Ed.* **2014**, *53*, 1; c) H. D. Lim, K. Y. Park, H. Song, E. Y. Jang, H. Gwon, J. Kim, Y. H. Kim, M. D. Lima, R. O. Robles, X. Lepro, R. H. Baughman, K. Kang, *Adv. Mater.* **2013**, *25*, 1348; d) Z. L. Wang, D. Xu, J. J. Xu, L. L. Zhang, X. B. Zhang, *Adv. Funct. Mater.* **2012**, *22*, 3699; e) Z. Guo, D. Zhou, X. Dong, Z. Qiu, Y. Wang, Y. Xia, *Adv. Mater.* **2013**, *25*, 5668.

[4] a) X. Huang, H. Yu, H. Tan, J. Zhu, W. Zhang, C. Wang, J. Zhang, Y. Wang, Y. Lv, Z. Zeng, D. Liu, J. Ding, Q. Zhang, M. Srinivasan, P. M. Ajayan, H. H. Hng, Q. Yan, *Adv. Funct. Mater.* **2014**, *24*, 6516; b) Q. Li, P. Xu, W. Gao, S. Ma, G. Zhang, R. Cao, J. Cho, H. L. Wang, G. Wu, *Adv. Mater.* **2014**, *26*, 1378; c) Z. Zhang, L. Su, M. Yang, M. Hu, J. Bao, J. Wei, Z. Zhou, *Chem. Commun.* **2014**, *50*, 776; d) J. Xiao, D. Mei, X. Li, W. Xu, D. Wang, G. L. Graff, W. D. Bennett, Z. Nie, L. V. Saraf, I. A. Aksay, J. Liu, J. G. Zhang, *Nano Lett.* **2011**, *11*, 5071; e) F. Li, Y. Chen, D. M. Tang, Z. Jian, C. Liu, D. Golberg, A. Yamada, H. Zhou, *Energy Environ. Sci.* **2014**, *7*, 1648; f) W. H. Ryu, T. H. Yoon, S. H. Song, S. Jeon, Y. J. Park, I. D. Kim, *Nano Lett.* **2013**, *13*, 4190.

[5] a) J. Shui, F. Du, C. Xue, Q. Li, L. Dai, *ACS Nano* **2014**, *8*, 3015; b) S. Liu, Y. Zhu, J. Xie, Y. Huo, H. Y. Yang, T. Zhu, G. Cao, X. Zhao, S. Zhang, *Adv. Energy Mater.* **2014**, *4*, 1301960; c) J. Park, Y. S. Jun, W. Lee, J. A. Gerbec, K. A. See, G. D. Stucky, *Chem. Mater.* **2013**, *25*, 3779; d) Y. Qin, J. Lu, P. Du, Z. Chen, Y. Ren, T. Wu, J. T. Miller, J. Wen, D. J. Miller, Z. Zhang, K. Amine, *Energy Environ. Sci.* **2013**, *6*, 519; e) R. R. Mitchell, B. M. Gallant, C. V. Thompsona, S. H. Yang, *Energy Environ. Sci.* **2011**, *4*, 2952.

[6] a) A. L. M. Reddy, A. Srivastava, S. R. Gowda, H. Gullapalli, M. Dubey, P. M. Ajayan, *ACS Nano* **2010**, *4*, 6337; b) L. Qu, Y. Liu, J. B. Baek, L. Dai, *ACS Nano* **2010**, *4*, 1321; c) Z. S. Wu, W. Ren, L. Xu, F. Li, H. M. Cheng, *ACS Nano* **2011**, *7*, 5463; d) C. Zhang, N. Mahmood, H. Yin, F. Liu, Y. Hou, *Adv. Mater.* **2013**, *25*, 4932; e) Y. Su, Y. Zhang, X. Zhuang, S. Li, D. Wu, F. Zhang, X. Feng, *Carbon* **2013**, *62*, 296; f) C. M. Chen, Q. Zhang, C. H. Huang, X. C. Zhao, B. S. Zhang, Q. Q. Kong, M. Z. Wang, Y. G. Yang, R. Cai, D. Sheng Su, *Chem. Commun.* **2012**, *48*, 7149; g) Y. Li, J. Wang, X. Li, D. Geng, R. Li, X. Sun, *Chem. Commun.* **2011**, *47*, 9438; h) Y. Cao, Z. Wei, J. He, J. Zang, M. Zheng, Q. Dong, *Energy Environ. Sci.* **2012**, *5*, 9765.

[7] a) Y. Li, J. Chen, L. Huang, C. Li, J. D. Hong, G. Shi, *Adv. Mater.* **2014**, *26*, 4789; b) W. Wei, S. Yang, H. Zhou, I. Lieberwirth, X. Feng,

K. Mullen, *Adv. Mater.* **2013**, *25*, 2909; c) Y. Xue, J. Liu, H. Chen, R. Wang, D. Li, J. Qu, L. Dai, *Angew. Chem. Int. Ed.* **2012**, *51*, 12124; d) Y. Zhao, C. Hu, Y. Hu, H. Cheng, G. Shi, L. Qu, *Angew. Chem. Int. Ed.* **2012**, *51*, 11371; e) X. Huang, B. Sun, D. Su, D. Zhao, G. Wang, *J. Mater. Chem. A* **2014**, *2*, 7973.

[8] Y. Xu, Z. Lin, X. Huang, Y. Wang, Y. Huang, X. Duan, *Adv. Mater.* **2013**, *25*, 5779.

[9] Y. Zhao, J. Liu, Y. Hu, H. Cheng, C. Hu, C. Jiang, L. Jiang, A. Cao, L. Qu, *Adv. Mater.* **2013**, *25*, 591.

[10] a) X. Lin, L. Zhou, T. Huang, A. Yu, *J. Mater. Chem. A* **2013**, *1*, 1239; b) J. Li, H. Zhang, Y. Zhang, M. Wang, F. Zhang, H. Nie, *Nanoscale* **2013**, *5*, 4647; c) J. J. Xu, Z. L. Wang, D. Xu, L. L. Zhang, X. B. Zhang, *Nat. Commun.* **2013**, *4*, 2438.

[11] a) Z. Zhang, J. Bao, C. He, Y. Chen, J. Wei, Z. Zhou, *Adv. Funct. Mater.* **2014**, *24*, 6826; b) Y. Li, J. Wang, X. Li, D. Geng, M. N. Banis, R. Li, X. Sun, *Electrochem. Commun.* **2012**, *18*, 12; c) Y. Li, J. Wang, X. Li, D. Geng, M. N. Banis, Y. Tang, D. Wang, R. Li, T. K. Sham, X. Sun, *J. Mater. Chem.* **2012**, *22*, 20170.

[12] Z. Niu, J. Chen, H. H. Hng, J. Ma, X. Chen, *Adv. Mater.* **2012**, *24*, 4144.

[13] H. Wang, C. Zhang, Z. Liu, L. Wang, P. Han, H. Xu, K. Zhang, S. Dong, J. Yao, G. Cui, *J. Mater. Chem.* **2011**, *21*, 5430.

[14] S. Liu, Z. Wang, C. Yu, Z. Zhao, X. Fan, Z. Ling, J. Qiu, *J. Mater. Chem. A* **2013**, *1*, 12033.

[15] B. Sun, X. Huang, S. Chen, P. Munroe, G. Wang, *Nano Lett.* **2014**,*14*, 3145.

[16] a) H. J. Peng, J. Q. Huang, M. Q. Zhao, Q. Zhang, X. B. Cheng, X. Y. Liu, W. Z. Qian, F. Wei, *Adv. Funct. Mater.* **2014**, *24*, 2772; b) P. Simon, Y. Gogotsi, *Nat. Mater.* **2008**, *7*, 845.

[17] Y. Chen, F. Li, D. M. Tang, Z. Jian, C. Liu, D. Golberg, A. Yamadac, H. Zhou, *J. Mater. Chem. A* **2013**, *1*, 13076.

[18] W. S. Hummers, R. E. Offeman, *J. Am. Chem. Soc.* **1958**, *80*, 1339.

[19] J. A. Lee, S. T. Ha, H. K. Choi, D. O. Shin, S. O. Kim, S. H. Im, O. O. Park, *Small* **2011**, *7*, 2581.